Notable Events

An overview of the Feb 27, 2010 Mw 8.8 Maule, Chile earthquake sequence

Gavin P. Hayes

National Earthquake Information Center,
United States Geological Survey

Golden, CO, USA

Excerpt from the
Summary of the Bulletin of the International Seismological Centre:

Hayes, G. P., An overview of the Feb 27, 2010 Mw 8.8 Maule, Chile earthquake sequence, *Summ. Bull. Internatl. Seismol. Cent.*, January - June 2010, *47*(1–6), pp. 88–103, Thatcham, United Kingdom, 2013, doi:10.5281/zenodo.998651.

8.2 An overview of the Feb 27, 2010 Mw 8.8 Maule, Chile earthquake sequence

Gavin P. Hayes
National Earthquake Information Center
United States Geological Survey
Golden, CO.
USA

8.2.1 Introduction

On February 27, 2010, at 06:34:14 UTC (03:34 at the epicenter), the Mw 8.8 Maule earthquake ruptured an approximately 400 km long section of the South American subduction zone in south-central Chile (epicentral location 36.12°S, 72.90°W, depth 22 km; USGS NEIC, http://on.doi.gov/yKhpUb). The earthquake occurred along the subduction interface separating the Nazca and South American plates, where oceanic lithosphere of the Nazca plate obliquely subducts beneath South America at a rate of approximately 7.4 cm/yr (DeMets *et al.*, 2010). This event caused extensive damage to nearby coastal cities and excited a large near- and far-field tsunami, the former of which caused localized run-up as high as 29 m near Constitución (Fritz *et al.*, 2011). Aftershocks of the earthquake covered an area approximately 700x300 km^2 in size, slightly overlapping the northern extent of the great 1960 Mw 9.5 Chile earthquake to the south, and the southern extent of the 1985 M 8.2 Central Chile earthquake to the north.

Before the Maule earthquake, the plate interface extending ~150 km south of the mainshock hypocenter, which had been referred to as the South Central Chile seismic gap (Ruegg *et al.*, 2009), had not slipped co-seismically in a large earthquake since a M 8.5 megathrust earthquake in 1835 (Figures 8.4 & 8.5). The region north of the hypocenter, on the other hand, had partially failed during large earthquakes in 1906 (M 8.4), 1928 (M 8.0) and in 1985 (M 8.2) (e.g., Beck *et al.*, 1998). Recent geodetic studies reveal that the plate interface between 38.0°S to 35.5°S was nearly fully locked during the six year period from 1996 to 2002 (Ruegg *et al.*, 2009; Moreno *et al.*, 2010).

The USGS W-phase (Kanamori and Rivera, 2008; Hayes *et al.*, 2009; Duputel *et al.*, 2011, Deputel *et al.*, 2012) centroid moment tensor (CMT) solution (http://on.doi.gov/z5LHcG) indicates the earthquake ruptured a shallow thrust fault that aligns well with the geometry of the slab up-dip of the hypocenter (Figure 8.4), with a best double-couple fault plane of strike $\varphi = 016°$, dip $\delta = 14°$, and rake $\lambda = 104°$. This solution has a seismic moment of $M_o = 2.00 \times 10^{29}$ dyne-cm. The CMT solution of the global Centroid Moment Tensor project (GCMT; http://www.globalcmt.org, Ekström *et al.*, 2012) has a seismic moment of $M_o = 1.86 \times 10^{29}$ dyne-cm, in close agreement with the W-phase moment, though with a slightly steeper dip ($\delta = 18°$). These solutions indicate that this earthquake, at the time, represented the fifth-largest event recorded during the modern era of instrumental seismology (eclipsed since by the March 11, 2011 Mw 9.0 Tohoku earthquake; Hayes, 2011; Hayes *et al.*, 2011; http://on.doi.gov/X4d1J1).

In this paper I present an overview of the source characteristics of this mega-earthquake and the tectonic framework of its aftershocks, inferred from studies involving this author (e.g., Hayes *et al.* 2012b, in

review) and from other published investigations (e.g., Rietbrock *et al.*, 2012; Lange *et al.*, 2012; Ryder *et al.*, 2012; etc). This work is thus meant to provide a review of our current understanding of this earthquake sequence, and its implications for future events along this portion of the South America megathrust plate boundary.

8.2.2 Mainshock Source Characteristics

In the hours and days following the Maule earthquake, several different groups published finite fault models describing the slip distribution of this event based on seismic data (e.g., Hayes, 2010; Shao *et al.*, 2010; Sladen, 2010). Since then, many more models have been published with various combinations of seismic, GPS, geologic, tsunami and InSAR data (e.g., Lay *et al.*, 2010; Delouis *et al.*, 2010; Tong *et al.*, 2011; Lorito *et al.*, 2011; Pollitz *et al.*, 2011; Vigny *et al.*, 2011). Those models generally infer earthquake source characteristics at relatively low frequencies, when inverting seismic data, or directly infer fault displacement when using geodetics. The models can also be kinematic (again, if they are using seismic data), thereby providing information on the time-history of the rupture process, or are static only (when using geodetic offsets). Some authors (e.g., Lay *et al.*, 2010; Kiser & Ishii, 2011; Wang & Mori, 2011; Lay *et al.*, 2012) have also analyzed the source characteristics of the earthquake at higher frequencies using the back-projection of body waves, as discussed further below.

Vigny *et al.* (2011) compare how most of the finite fault models published at the time of their study fit a dense suite of GPS displacement vectors from the epicentral region of the earthquake, collected as both continuous and campaign data. While their model (constructed via an inversion of the GPS vectors) fits these data best, they show that the USGS model (Hayes, 2010) fit the data reasonably well, and better than the other seismic-only models. The majority of the misfit between the Hayes (2010) model and the GPS data comes from a lack of slip in the southern part of the rupture area, also a problem in the other seismic-only solutions.

Vigny *et al.* (2011) also note their favored low-frequency earthquake onset is shifted approximately 50 km southwest of the USGS-NEIC hypocenter. Rupture velocities for the earthquake were variably reported as 1.75-2.75 km/s (Hayes, 2010); 2.0-2.5 km/s (Lay *et al.*, 2010); averaging 2.6 km/s but as high as 3.2 km/s (Delouis *et al.*, 2010); and 3.1 km/s (Vigny *et al.*, 2011). Finally, most models used a single-plane geometry for their inversion (with the exception of Lorito *et al.*, 2011), though some did explore the affect of changing the assumed dip angle for both single (Lay *et al.*, 2010; Pollitz *et al.*, 2011) and multiple (Lay *et al.*, 2010) planes. Each models' geometry was based on approximate fits to the local subduction zone and/or the GCMT solution, using dips varying from 15°-18° (for single-planes).

Hayes *et al.* (2012b) conduct an in-depth reanalysis of their original teleseismic inversion, aimed at resolving some of these discrepancies between various published models by more fully exploring the parameter space of the inversion procedure. In particular, they examine the effects of better accounting for the variation in slab geometry over the rupture by dividing the model space into several individual planes. Their results show that, while single-, three-, and five-plane models can all fit teleseismic data reasonably well (explaining 88-90% of the inverted data), the same models produce significant differences in fits to regional GPS data. Conversely, this implies that improvements in fits to GPS data are made with stepwise improvements to the assumed fault geometry; in other words, careful consideration of slab

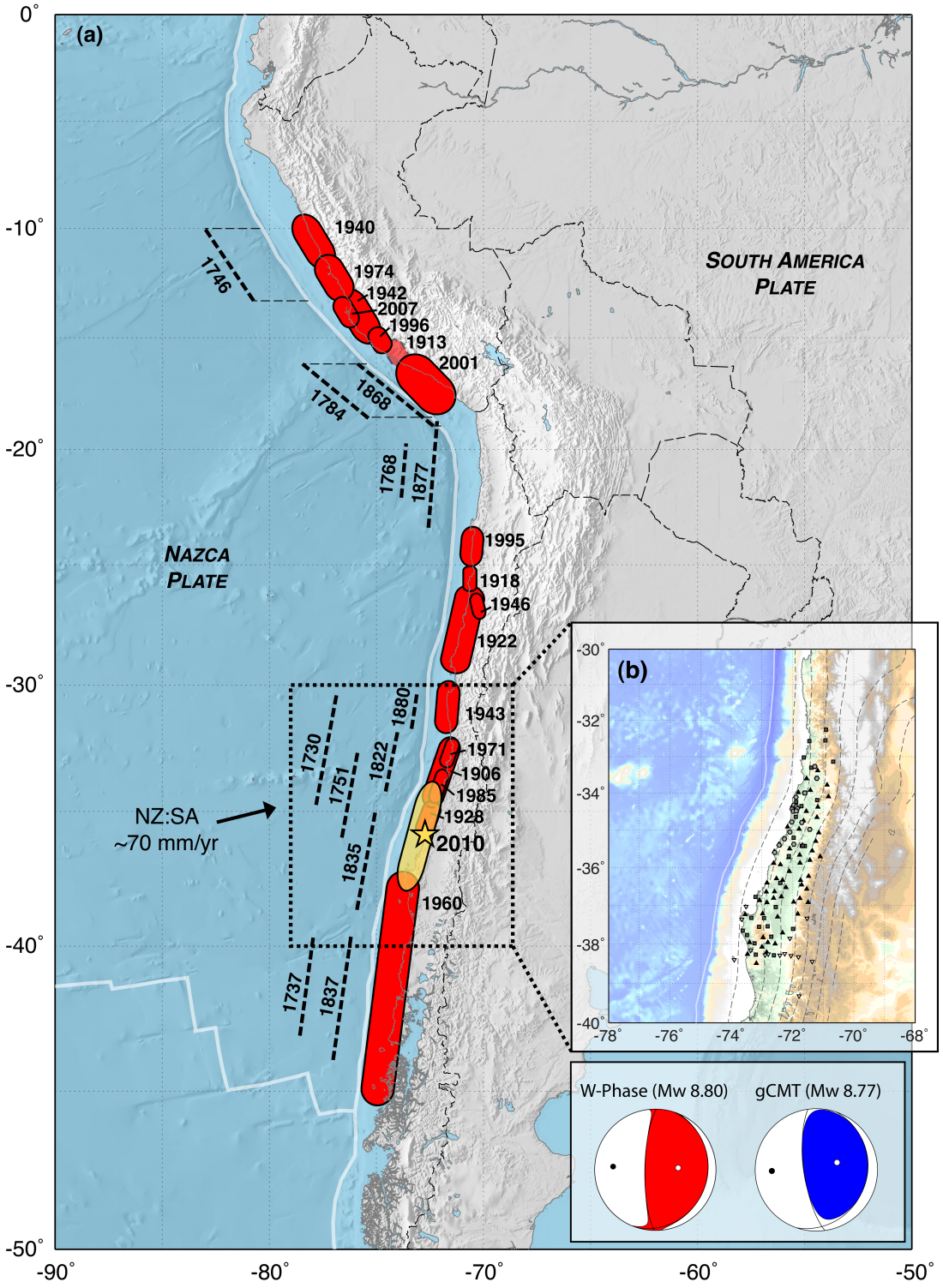

Figure 8.4: *Tectonic setting of the February 27, 2010 Mw 8.8 Maule earthquake. (a) shows the seismologic history of the South America subduction zone; Major 20th century ruptures are shown with red polygons representing their approximate rupture extent, following Beck et al., (1998). Approximate rupture lengths of major pre-20th century earthquakes are shown with black lines outboard of the subduction zone for clarity. The extent of the 2010 rupture is illustrated with a yellow polygon; the star represents the earthquake epicenter. CMT mechanisms for the mainshock are given in the inset. The black arrow represents Nazca:South America plate motion of 70 mm/yr. The dashed black box shows the extent of all subsequent figures, and of (b), which shows stations from the IMAD aftershock deployment. Different symbols represent the operating institution; black triangles are IRIS (US) stations, inverted white triangles UK, dark gray squares French, and hexagons German. Background bathymetric data, here and in subsequent figures, is taken from the GEBCO_08 grid, version 20100927, http://www.gebco.net).*

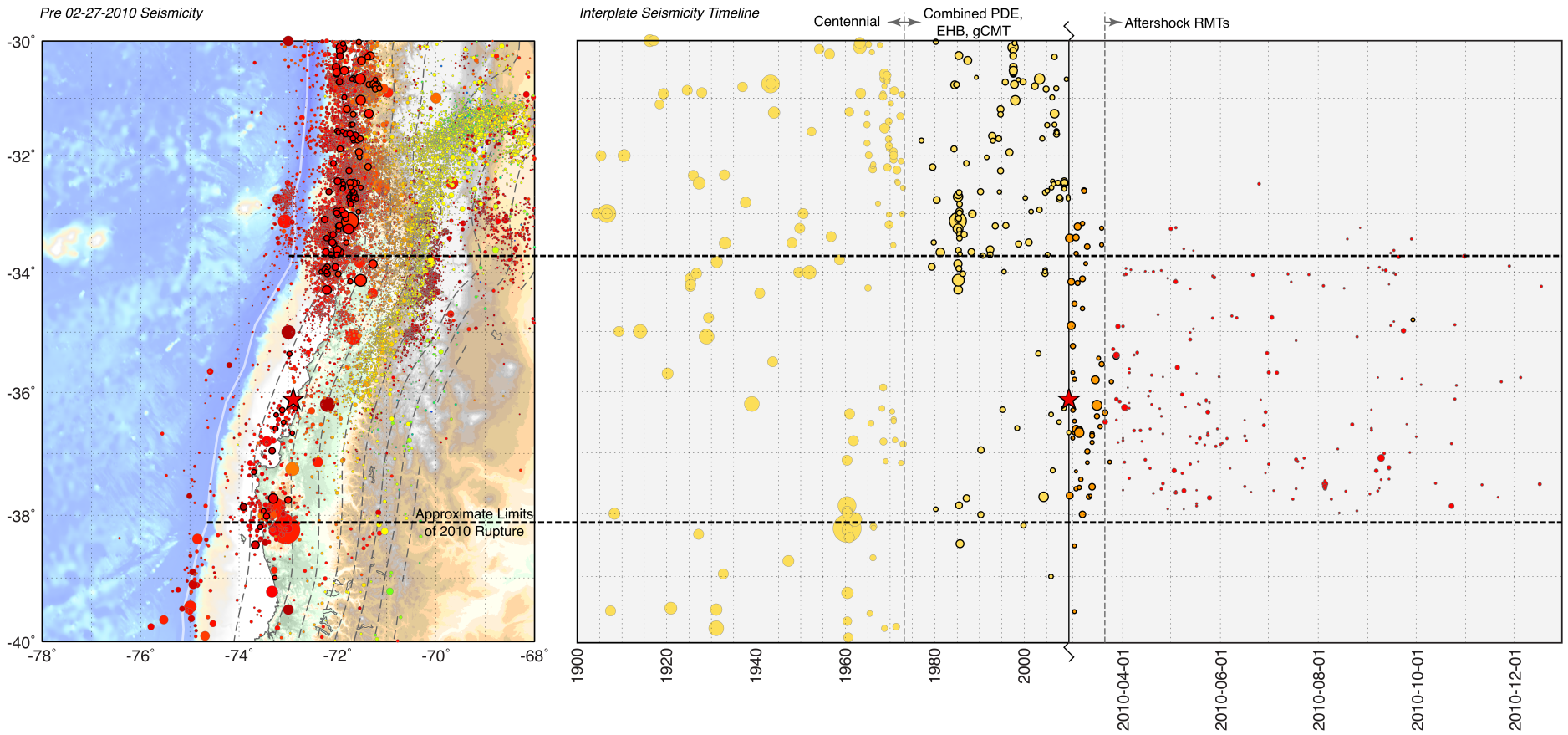

Figure 8.5: *(a) Pre- February 27, 2010 seismicity in the Centennial (Villeseñor and Engdahl, 2002; plotted 1900-1973), EHB (Engdahl et al., 1998; plotted 1973-present) and USGS PDE (plotted 1973-present, for those events without EHB locations) catalogs. Earthquake symbols are sized by magnitude and colored by depth. Those shown with thicker black outlines represent interplate earthquakes, discriminated via a comparison of their hypocenters and associated GCMT mechanisms to the Slab1.0 subduction zone model for the region (see text for details). Slab1.0 model contours are shown with dashed gray lines. The location of the February 27, 2010 epicenter is shown with a star. Approximate rupture limits are illustrated with dashed black lines. In (b), I show a timeline of Centennial catalog (pre-1976) and interplate seismicity (post-1976, the beginning of the GCMT catalog) in the source region of the Maule earthquake, showing the relative quiescence of the rupture area prior to the 2010 rupture. Yellow circles with light gray outlines are Centennial catalog events; yellow circles with thicker black outlines are EHB/PDE/GCMT catalog interface events. Orange circles represent post-mainshock events from the PDE catalog, while red circles represent aftershocks used in this study. Both of these later two data sets have also been filtered according to either their GCMT (for PDE/orange events) or RMT (for regional aftershocks/red events) mechanism to identify interplate earthquakes.*

geometry can improve seismic data inversions to levels comparable to many inversions based on the local and regional geodetic data, without the specific inclusion of those data in the inversion process.

The importance of geometrical control on resulting slip distributions is discussed further – and perhaps dealt with most satisfactorily – by Moreno *et al.* (2012), who use a three-dimensional fault geometry in a spherical-earth finite-element model to solve for a static slip distribution using regional GPS data. As discussed below, their resulting model is very similar to those of Hayes *et al.* (2012b) and Vigny *et al.* (2011). Moreno *et al.* (2012) goes on to compare co-seismic slip distributions for the 2010 earthquake to estimates of pre-event interface coupling, in a similar manner to Moreno *et al.* (2010), and Lorito *et al.* (2011), who reached opposing conclusions – the former implying a pre-event Constitución seismic gap had been filled, and the latter inferring it had not. This more detailed and updated Moreno *et al.* (2012) analysis confirms the earlier findings of Moreno *et al.* (2010) – that this gap was most likely closed by the Maule earthquake – and indeed that the 2010 slip may have been larger than that which had accumulated since the last megathrust earthquake in the region in 1835, implying either some local overshoot or inherited slip deficit in the region from strain accumulation before 1835.

Resulting favored slip distributions – in the Hayes *et al.* (2012b; Figure 8.6), Vigny *et al.* (2011), and Moreno *et al.* (2012) models – are similar, and indicate rupture dominated by two or three major asperities, in the northern shallow trench near 35°S, and in the south near 36°S-37°S (this slip patch is slightly further north in the Hayes model, and is separated into two smaller patches in the Moreno model). The Hayes model also shows a third asperity south of and along strike from the hypocenter just off the coast, down-dip from the second asperity, and covering a larger area than a similar feature in the Vigny model. In all models, peak slips reach approximately 15-20 m. These three models also imply a convergence of solutions showing offshore slip was dominant in this earthquake, in contrast to some other previous models favoring slip on the deeper portion of the megathrust (e.g., Lorito *et al.*, 2011), an inconsistency raised and discussed in more detail in Rietbrock *et al.* (2012).

Another interesting feature of the Hayes and Vigny models is a prominent slip minima very close to the hypocenter – up-dip and to the west-northwest in the Hayes model, and west-southwest in the Vigny model. In the latter model, this "anti-asperity" co-locates with after-slip derived in Vigny *et al.* (2011): in the former model, with the approximate rupture area of the M 8.0 1928 megathrust earthquake (Figure 8.4), though the precise slip distribution of that event is unclear. The small difference in the location of this low-slip region in each of these models may be related to the differences in hypocentral location, which is further south in Vigny *et al.* (2011). In the kinematic models of Hayes *et al.* (2012b), the hypocenter is used as the point of rupture initiation, thus influencing the resulting locations of slip on the modeled fault plane. Moreno *et al.* (2012) use a hypocenter closer to the Hayes model, derived from relocations of the mainshock and aftershock sequence as discussed in the following section.

As previously mentioned, several models of high-frequency rupture propagation have also been published via the use of the back-projection technique (Lay *et al.*, 2010; Kiser & Ishii, 2011; Wang & Mori, 2011; Lay *et al.*, 2012). In general, these studies favor rupture models dominated by northward rupture propagation, though both Kiser & Ishii (2011) and Wang & Mori (2011) also identify rupture south of the hypocenter, with dominant frequencies much lower than those related to rupture further north. Wang & Mori (2011) suggest these characteristics may be reflective of the coupling properties of the megathrust prior to the earthquake, such that areas of high coupling may cause greater heterogeneity in

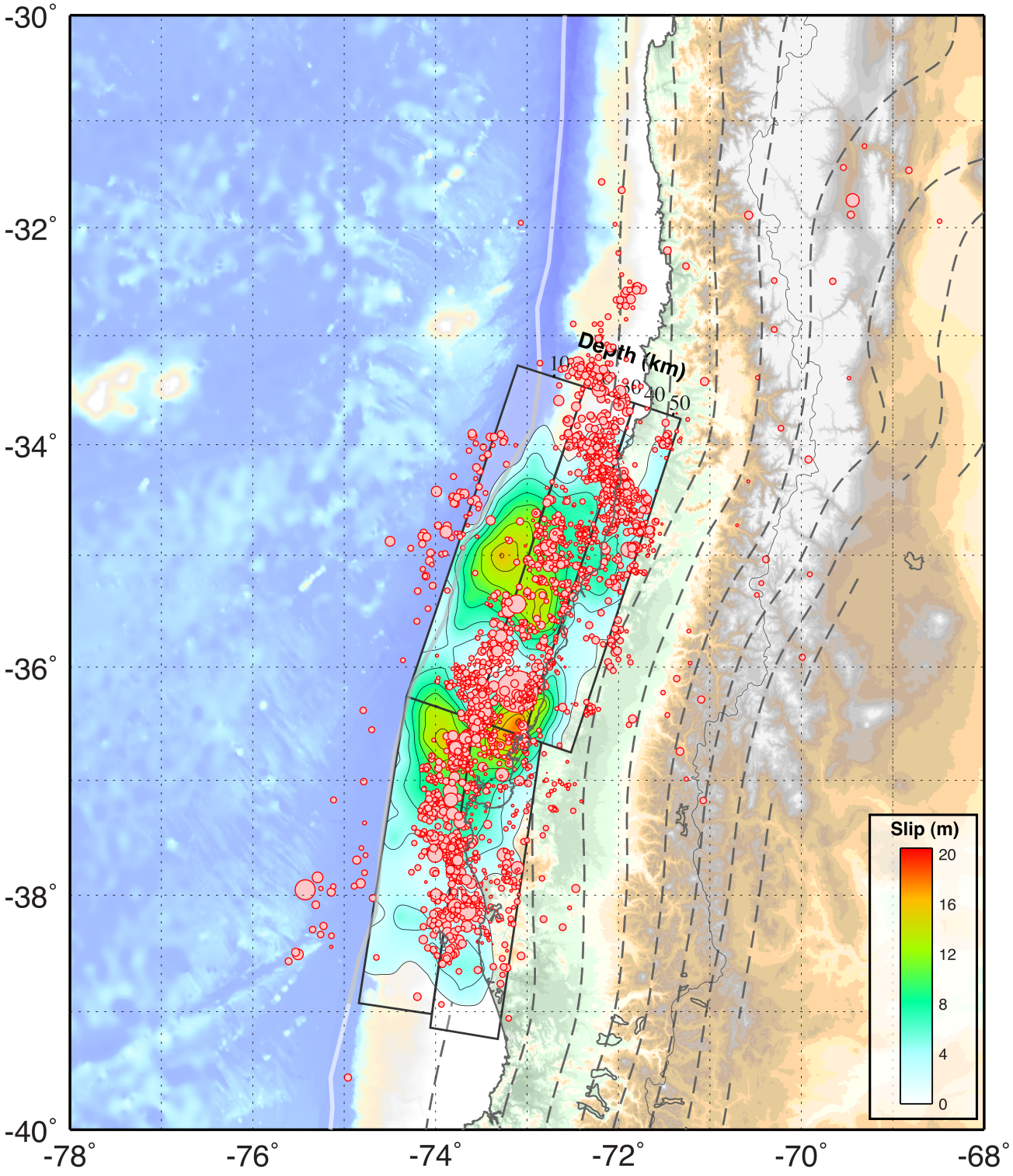

Figure 8.6: *Favored co-seismic slip model from Hayes et al. (2012b), from the inversion of teleseismic data over five planes (black rectangles encompassing slip distribution) approximating the subduction zone interface (gray dashed contours, from Slab1.0, Hayes et al., 2012a). Slip is contoured in 4m intervals. Overlain on this slip model is the relocated aftershock catalog of approximately 2,500 events from the same study, sized by magnitude. The thick transparent white line represents the inferred location of the Nazca:South America plate boundary.*

fault properties and have higher overall stress, resulting in more efficient high frequency energy radiation during subsequent earthquakes. Issues of frequency-dependent rupture properties of the megathrust have been explored in more detail by Lay *et al.* (2012), after the extremely interesting observation during the Mw 9.0 Tohoku, Japan earthquake that high-frequency energy radiation was predominantly located along deeper portions of the plate interface than was the low frequency radiation and dominant fault slip. They find similar patterns of depth variation in seismic wave radiation for the Maule earthquake, and for the 2004 Mw 9.1 Sumatra earthquake, implying such features may be characteristic of megathrust earthquakes, and highlighting the necessity for studies of earthquake rupture properties across a broad range of frequencies.

8.2.3 Studies of the Aftershock Sequence

In the weeks following the Maule earthquake, an unprecedented international collaboration involving teams and instruments from Chilean Universities, the Incorporated Research Institutions for Seismology (IRIS) in the US, the Institut National des Sciences de l'Univers of the Centre National de la Recherche Scientifique (INSU, CNRS) in France, Geo Forschungs Zentrum Posdam (GFZ) in Germany, and the University of Liverpool in the UK was established to deploy the International Maule Aftershock Deployment (IMAD) temporary network. Over 160 mostly broadband sensors were deployed over the on-land extent of the earthquake source region (Figure 8.6). Data from almost all of these stations were made available immediately following their collection through IRIS and GFZ, spanning March-December, 2010.

Several published studies have produced catalogs of this aftershock sequence, both from automatic picking of the datasets (e.g., Rietbrock *et al.*, 2012; Lange *et al.*, 2012) and from higher-resolution (and conversely lower event density) earthquake relocation analysis (Hayes *et al.*, 2012b). Analyses of aftershock source processes have also been published, using dominantly teleseismic (Aguerto *et al.*, 2012) and denser regional (Hayes *et al.*, 2012b) moment tensor data sets.

Through the automatic picking and processing of the first six months of IMAD data, Lange *et al.* (2012) located over 20,000 aftershocks in the source region of the Maule earthquake. They identify several distinct tectonic settings active during this period: 1) earthquakes in a region they call the outer rise, outboard of the subduction zone and adjacent to the mainshock rupture; 2) plate interface seismicity in or adjacent to the regions of highest co-seismic slip; 3) seismicity in a cluster at the deeper limit of interface seismogenesis below the mainshock rupture zone, and thus likely associated with after-slip; 4) earthquakes at intermediate (80-120 km) depths, within the subducting slab; and 5) earthquakes in the upper plate at the northern end of the rupture along crustal faults oblique to the subduction zone, associated with two major normal faulting aftershocks on March 11, 2010. These authors note that comparisons between aftershock locations and slip are dependent on the slip model used in the comparison – in other words, reliability of the source inversion procedure and thus of the resulting model is an important factor in studying such correlations. Comparisons of their aftershock catalog to the Vigny *et al.* (2011) model show aftershock activity predominantly down-dip of the regions of highest co-seismic slip.

The Rietbrock *et al.* (2012) study also uses automated picking and processing algorithms, and builds a catalog of over 30,000 earthquakes occurring over just the first two months of the IMAD deployment. This

study also attempts to improve upon the accuracy of automated detection algorithms by incorporating S-wave arrivals, and by using a two dimensional velocity model. Resulting locations from the Rietbrock catalog agree well with those from Lange *et al.* (2012), identifying aftershock activity outboard of the subduction zone with the oceanic plate, in two distinct clusters along the subduction zone thrust, and within the upper plate surrounding the Pichilemu region, where the March 11, 2010 normal faulting aftershocks occurred. This study goes on to use aftershock distributions to discriminate between slip models of varying quality, based on the assumption that aftershocks should generally occur in areas of rapid transition between high and low slip, surrounding (but not co-located with) areas of high slip. Under such a premise, the slip model of Vigny *et al.* (2011) is preferred over those of (for example) Lorito *et al.* (2011) and Delouis *et al.* (2010), because aftershocks locate at the down-dip extent of shallow high-slip regions, rather than somewhat coincident with highest slip. Their findings support a model where aftershocks occur predominantly in the transitional regions between high and low slip, rather than preferentially in areas of lowest slip.

The Aguerto *et al.* (2012) study builds on the catalog produced by Rietbrock *et al.* (2012), analyzing the largest events to produce a catalog of approximately 125 regional moment tensor (RMT) solutions. They also relocate centroid moment tensor (CMT) solutions from the global CMT catalog (http://www.globalcmt.org), adding almost 150 further moment tensors to their dataset. Using this catalog, they infer that most large aftershocks (70%) occur on the subduction thrust interface. Like Rietbrock *et al.* (2012), Aguerto *et al.* (2012) conclude that such events occur predominantly away from the areas of highest co-seismic slip, based on comparisons to the slip model of Moreno *et al.* (2012). Interestingly, they also note that, in contrast to their findings for large events, small (M<4) aftershocks predominantly occur where co-seismic slip is highest, possibly as a result of processes occurring in the damage zone around the megathrust interface.

These studies highlight the importance of an accurate source inversion for comparisons of aftershock distributions to co-seismic slip. Also vital for such studies is confidence in the accuracy of aftershock locations. Hayes *et al.* (2012b) attempt to address both issues by relocating the largest aftershocks (producing a catalog of over 2000 well-located earthquakes, with horizontal uncertainties averaging +/- 2.8 km; Figure 8.6), and carefully analyzing modeling parameters in kinematic source inversions with teleseismic data, aided by the forward modeling of regional GPS signals, as discussed above. They derive a model (Figure 8.6) that fits both the teleseismic data and the available regional GPS data better than most other published source models (which predominantly use GPS and InSAR data when conducting joint inversions, thereby solving for the static and not the kinematic rupture history), and derive an aftershock catalog which, while smaller than those of Lange *et al.* (2012) and Reitbrock *et al.* (2012), provides precise locations that can be confidently used for the detailed analysis of aftershock distributions with respect to co-seismic slip.

In addition, Hayes *et al.* (2012b) derive RMTs for 475 of the largest aftershocks (Figure 8.7), directly tied in to the rest of the relocated aftershock sequence, and categorize those events by their occurrence in the upper and lower-plates or on the subduction thrust interface based on comparisons to the Slab1.0 subduction zone geometry model (Hayes *et al.*, 2012a). Their analyses show that, if one classifies thrust interface earthquakes in a similar manner to Asano *et al.* (2011) and filters moment tensors by depth difference from the slab (±10 km), mechanism type (thrust) and rotation angle from the interface

geometry (within a Kagan angle of 35°; Kagan 1991), then just over 50% of the 475 aftershocks with RMTs can be classified as occurring on the plate boundary. Following the approach taken by Aguerto *et al.* (2012) and discriminating events on just mechanism type (thrust) and depth difference from the slab (±5 km), that number rises to 58%, in slight contrast to the figure of 70% found in Aguerto *et al.* (2012). Using the entire catalog rather than just the RMT dataset, 43% of events lie within ±5 km of the plate boundary. Like Aguerto *et al.* (2012), the Hayes *et al.* (2012b) study finds that the majority of the interplate after-slip occurs away from peaks in co-seismic slip, where slip is either low or relatively moderate with respect to co-seismic maxima. However, comparisons with co-seismic slip gradients show that aftershocks do not necessarily occur where changes in co-seismic slip were most rapid; in fact, most aftershocks locate where slip gradients are also moderate-to-low.

Also of interest in the Hayes *et al.* (2012b) study is that just 55% of aftershocks lie within regions of positive Coulomb stress (Lin & Stein, 2004) resulting from their favored co-seismic slip model, just slightly more than we might expect from a random distribution of aftershocks within the mainshock rupture area. This is likely an artifact of the high sensitivity of Coulomb stress transfer calculations on the precise distribution of co-seismic slip (which is calculated at a resolution of 25x18 km in the along-strike and down-dip directions, respectively), and uncertainties in aftershock locations (several kilometers horizontally and vertically); small changes in either can cause a switch from negative to positive Coulomb stress transfer (Ross Stein, pers. comm., 2012). In fact, considering just the range of vertical uncertainty of relocated aftershocks in Hayes *et al.* (2012b), the percentage of aftershocks locating in regions of positive stress transfer increases to approximately 70%. Incorporating horizontal uncertainties increases this further, to between 80% and 85%. This illustrates the care that must be taken in comparing aftershock distributions to models of co-seismic slip.

Cross-sections through the epicentral region of the mainshock and aftershock zone (Figure 8.8) show nicely the spatial distribution of the aftershock sequence, and the associated tectonic features they activate. RMTs indicate a dominance of thrust faulting close to the subduction zone interface. These cross-sections identify a set of events near the base of the seismogenic zone (e.g., A-A', B-B', D-D') that is spatially distinct from other thrust aftershocks, and helps to define the depth extent of faulting on the plate interface in this region (at the deep limit of these events), as well as the depth-extent of co-seismic slip (at the shallow limit of these events). Cross-section D-D' highlights a sequence of upper plate earthquakes near the northern end of the mainshock rupture zone, dominated by normal faulting. These earthquakes are associated with two large M 7.0 and M 6.9 aftershocks on March 11, 2010, near Pichilemu. The sequence branches upward from and oblique to the subduction zone interface (strikes of the largest two events are approximately 145° and 155°; www.globalcmt.org), and seems to promote subsequent aftershock activity on the up-dip portion of the megathrust plate boundary (since all of our RMTs are associated with earthquakes subsequent to the Pichilemu events), while possibly inhibiting activity on the portion of the megathrust directly beneath the upper plate normal faults (Figure 8.8). Also visible in both cross-section and in map view (Figure 8.6) is aftershock activity within the oceanic plate outboard of the subduction zone, in two clusters at the northern and southern ends of the mainshock rupture. While the more dominant of these clusters, in the north, lies directly up-dip of the main co-seismic asperity, the southern cluster aligns more closely with fracture zones at the south end of the rupture, further south than the asperity between 36°S-37°S.

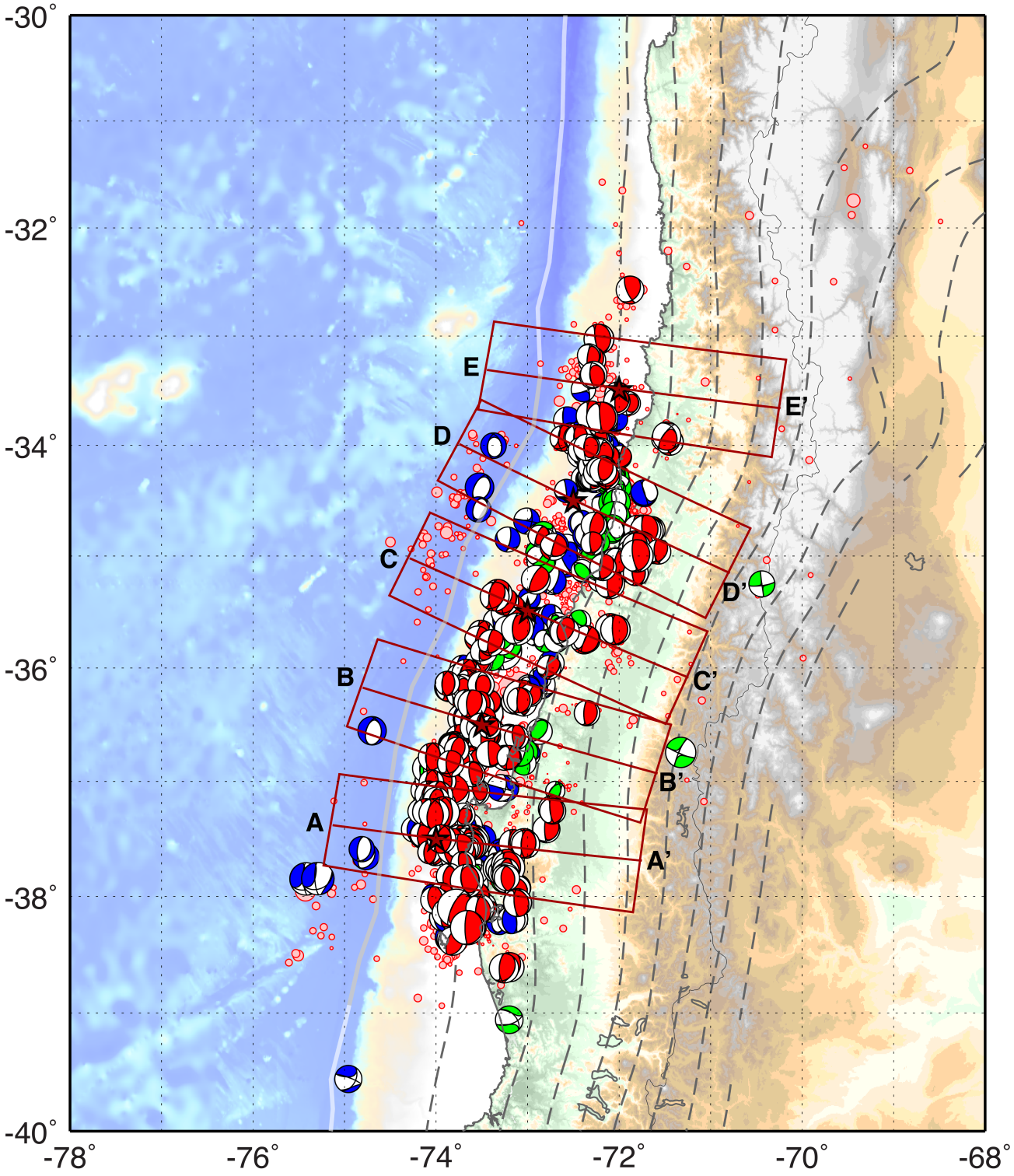

Figure 8.7: *Aftershock relocations and Regional Moment Tensors (RMTs), subdivided by their inferred tectonic environment (upper, lower, interplate; green, blue, red, respectively). Dark gray dashed contours represent the depth of the subducting Pacific slab in 20 km intervals, from Slab1.0 (Hayes et al., 2012a). The thick transparent white line represents the inferred location of the Nazca:South America plate boundary. Red lines show the boundaries of cross-sections in Figure 8.8.*

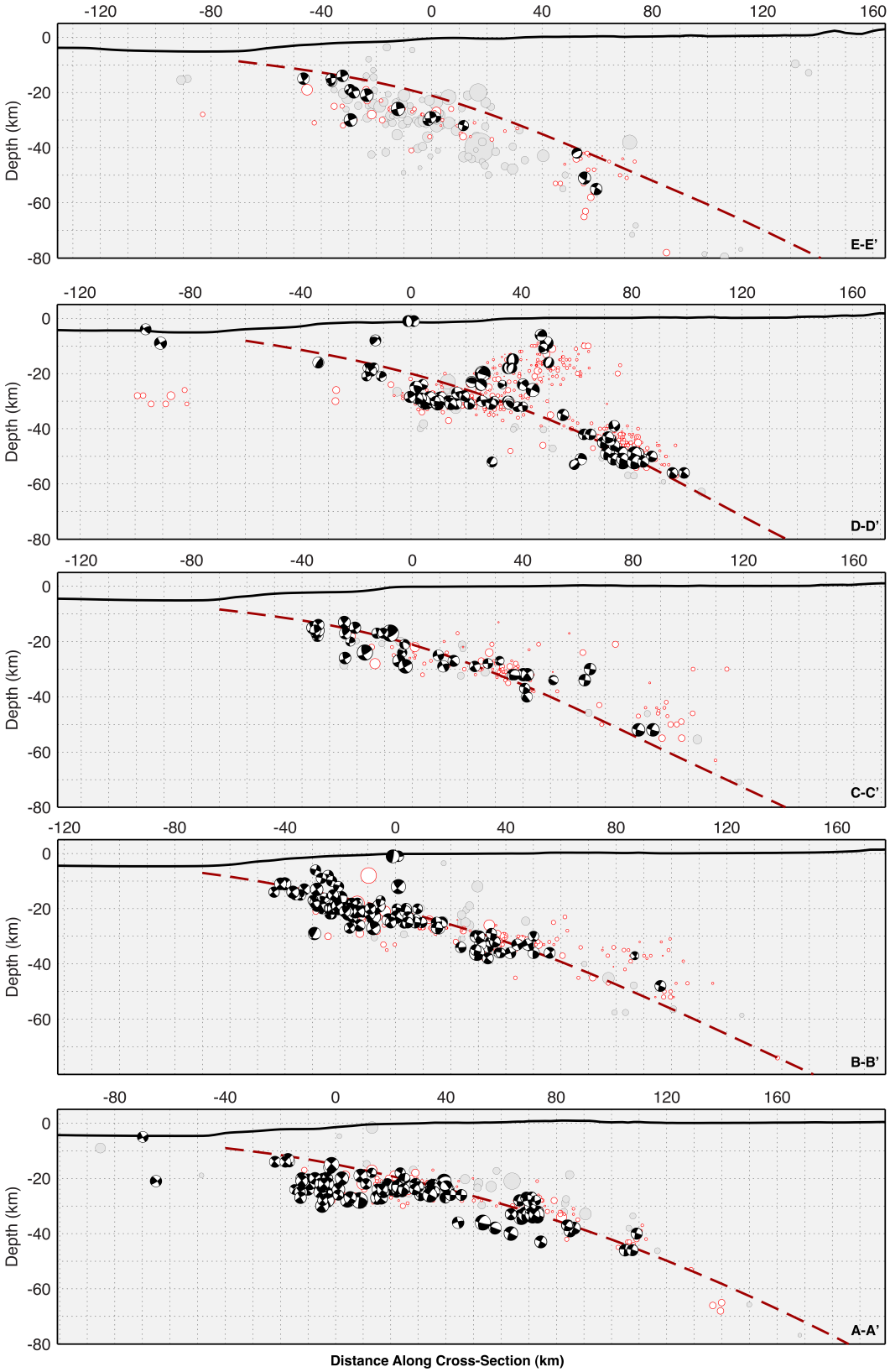

Figure 8.8: *Cross-sections through the aftershock sequence, showing the depth distribution of historic (light gray circles, thin black outlines) and aftershock (white circles, red outlines) seismicity, with symbols sized according to magnitude. RMTs of the aftershock sequence are also shown, as rear-hemisphere projections of the best fitting double-couple mechanism. Red dashed lines show the subduction zone interface location, from Slab1.0 (Hayes et al., 2012a). The black solid line near the surface shows bathymetry/topography, taken from GEBCO bathymetric data. Cross-sections are displayed from north (E-E') to south (A-A'). For cross-section locations, see Figure 8.7.*

8.2.4 Discussion

In this paper I summarize some of the more prominent findings derived from studies of the 2010 Maule earthquake, with a specific focus on work related to inversions of co-seismic slip, and catalogs of subsequent aftershock distributions and moment tensor analyses.

Published co-seismic slip models are numerous, derived from various combinations of one or more of teleseismic, GPS, InSAR and tsunami datasets. Many of the more recent models, such as Vigny *et al.* (2011), Moreno *et al.* (2012), and Hayes *et al.* (2012b), indicate dominantly offshore slip in two-to-three major asperities: north of the hypocenter near 35°S, and in the south near 36°S-37°S. Co-seismic slips reached 15-20 m, and the northern and southern asperities were separated by a prominent minima in slip near the hypocenter, close to the location of the M8.0 1928 megathrust earthquake. Interestingly, while these and other teleseismic and geodetically derived slip models favor slip on the shallower, offshore portions of the subduction thrust, those models including tsunami data (e.g., Lorito *et al.*, 2011; Fujii and Satake, 2012) derive slip beneath the coastline, somewhat at odds with measurements of coastal subsidence and uplift (Farias *et al.*, 2010). This discrepancy has yet to be satisfactorily resolved.

Several catalogs of aftershocks and regional moment tensors for the Maule earthquake sequence have also been published to date, taking advantage of the unprecedented multi-national deployment and open access data of the IMAD network in the months following the mainshock rupture. The more dense catalogs of Lange *et al.* (2012) and Rietbrock *et al.* (2012), derived from automated picking algorithms, provide details of the tectonic settings activated by the aftershock sequence, and highlight dependencies in correlations between co-seismic and aftershock slip on the co-seismic model chosen for that comparison. Both studies favor slip inversions that derive slip in the shallower subduction thrust environment (e.g., Vigny *et al.*, 2011), and thus infer that slip in the largest aftershocks (M4+) occurs on the fringes of high slip, in regions of transition from high-to-low co-seismic slip environments. This is also the conclusion reached by Aguerto *et al.* (2012), which quantify patterns in aftershock slip distributions and their relationship to co-seismic slip by using a moment tensor catalog made up of their own regional moment tensors, and a relocated set of centroid moment tensors from the GCMT catalog. A detailed relocation of the largest aftershocks, as well as a more extensive set of regional moment tensors from Hayes *et al.* (2012b), provide similar results. However, Hayes *et al.* (2012b) find that overall a smaller fraction of the aftershock sequence is represented by interplate thrusting (55% versus 70% in Aguerto *et al.*, 2012), and that of those subduction interface events, most occur in regions of low slip and low slip gradient, rather than specifically where slip gradients are high and transitioning away from major asperities. Importantly, Hayes *et al.* (2012b) also demonstrate that comparisons of aftershock locations and co-seismic slip for the purposes of Coulomb stress transfer calculations are extremely dependent on uncertainties in both – particularly in earthquake location – and as such errors in even relocated earthquakes need to be taken into account in such studies.

8.2.5 Conclusions

The 2010 Maule earthquake was, at the time of the event, the fifth-largest earthquake ever recorded in the modern instrumental era. Owing to the expansions in global and regional seismic and geodetic networks over the past several years-to-decades, and in particular since the 2004 M 9.1 (Park *et al.*,

2005) Sumatra earthquake, data from this event and its aftershock sequence were perhaps also the best on record (since eclipsed by the 2011 M 9.0 Tohoku earthquake, offshore from Japan). Because of this, and owing also to the advancements of processing techniques and understanding of the earthquake source that have accompanied such data expansions, the Maule earthquake has been studied across multiple time and frequency scales, providing results that are helping to change the way we understand megathrust earthquake slip across the inter-, co-, and post-seismic spectrum. Such datasets for this and other similar earthquakes (including the Tohoku event) are likely to continue to provide insights into the behavior of megathrust plate boundaries, insights which will in turn help shape the way we characterize and respond to earthquake hazards and their associated societal risks in the future.

8.2.6 Acknowledgements

The author wishes to thank Harley Benz, Eric Bergman, Robert Herrmann, Andres Rietbrock, Chen Ji and Sergio Barrientos for discussions related to the Maule earthquake and subsequent data analyses, and Paul Earle and Wayne Richardson for thorough reviews of an initial manuscript. The Seismological Service National de Chile, Universidad de Chile, Universidad de Concepción, IRIS, the University of Liverpool, CNRS-INSU, and GFZ were all instrumental in the deployment, operation and recovery of the IMAD network; without their extensive efforts many of the studies discussed in this paper would not have been possible. Many of the figures were made using GMT, and I thank their developers and the many users of their support list. Thanks also to the global Centroid Moment Tensor project group for the maintenance of and open access to their catalog.

8.2.7 References

Agurto, H., Rietbrock, A., Ryder, I., and Miller, M., 2012. Seismic-afterslip characterization of the 2012 Mw 8.8 Maule, Chile, earthquake, based on moment tensor inversion, Geophys. Res. Lett. 39, doi:10.1029/2012GL053434.

Asano, Y., Saito, T., Ito, Y., Shiomi, K., Hirose, H., Matsumoto, T., Aoi, S., Hori, S., and Sekiguchi, S., 2010. Spatial distribution and focal mechanisms of aftershocks of the 2011 off the Pacific Coast of Tohoku Earthquake, Earth Planets Space 63, 669-673.

Beck, S., Barientos, S., Kausel, E., and Reyes, M., 1998. Source characteristics of historic earthquake along the central Chile subduction zone, J. South Am. Earth Sci. 11, 115–129, doi:10.1016/S0895-9811(98) 00005-4.

Delouis, B., Nocquet, J-M., and Vallée, M., 2010. Slip distribution of the February 27, 2010 Mw = 8.8 Maule earthquake, central Chile, from static and high-rate GPS, InSAR, and broadband teleseismic data, Geophys. J. Lett. 37, L17305, doi:10.1029/2010GL043899.

DeMets, C., Gordon, R.G., and Argus, D.F., 2010. Geologically current plate motions, Geophys. J. Int. 181, 1-80, doi: 10.1111/j.1365-246X.2009.04491.x.

Duputel, Z., Rivera, L., Kanamori, H., Hayes, G.P., Hirshorn, B., and Weinstein, S., 2011. Real-time W Phase inversion during the 2011 off the Pacific Coast of Tohoku Earthquake, Earth Planets Space 63, 535–539.

Duputel, Z., Rivera, L., Kanamori, H., and Hayes, G., 2012. W phase source inversion for moderate to large earthquakes (1990–2010). Geophys. J. Int. 189, 1125–1147.

Ekström, G., Nettles, M., and Dziewoński, A.M., 2012. The global CMT project 2004-2010: Centroid-moment tensors for 13,017 earthquakes, Phys. Ear. Planet. Int. 200-201, 1-9.

Engdahl, R., and A. Villaseñor (2002), Global seismicity: 1900–1999, in International Handbook of Earthquake and Engineering Seismology, Part A, edited by W. H. K. Lee *et al.*, chap. 41, pp. 665–690, Academic, Amsterdam, doi:10.1016/S0074-6142(02)80244-3.

Engdahl, E. R., R. D. Van Der Hilst, and R. P. Buland (1998), Global teleseismic earthquake relocation with improved travel times and procedures for depth determination, Bull. Seis. Soc. Am., 88, 722–743.

Farias, M., Vargas, G., Tassara, A., Carretier, S., Baize, S., Melnick, D., and Bataille, K., 2010. Land-Level Changes Produced by the Mw 8.8 2010 Chilean Earthquake, Science, 329(5994), 916–916.

Fujii, Y., and Satake, K., 2012. Slip distribution and seismic moment of the 2010 and 1960 Chilean earthquakes inferred from tsunami waveforms and coastal geodetic data, Pure Appl. Geophys., doi:10.1007/s00024-012-0524-2.

Fritz, H. M., Petroff, C. M., Catalan, P. A., Cienfuegos, R., Winckler, P., Kalligeris, N., Weiss, R., Barrientos, S. E., Meneses, G., Valderas-Bermejo, C., Ebeling, C., Papadopoulos, A., Contreras, M., Almar, R., Dominguez, J. C., and Synolakis, C. E., 2011. Field survey of the 27 February 2010 Chile tsunami, Pure Appl. Geophys., doi:10.1007/s00024-00011- 00283-00025.

Hayes, G., 2010. Finite fault model, updated results of the Feb. 27, 2010 Mw 8.8 Maule, Chile earthquake, http://earthquake.usgs.gov/earthquakes/eqinthenews/2010/us2010tfan/finite_fault.php.

Hayes, G.P., 2011. Rapid source characterization of the 2011 Mw 9.0 off the Pacific coast of Tohoku earthquake, Earth Planets Space 63, 529-534.

Hayes, G.P., Rivera, L., and Kanamori, H., 2009. Source inversion of the W-Phase: real- time implementation and extension to low magnitudes. Seismol. Res. Lett. 80, 817–822.

Hayes, G.P., Earle, P.S., Benz, H.M, Wald, D.J., Briggs, R.W., and the USGS/NEIC Earthquake Response Team, 2011. 88 Hours: The U.S. Geological Survey National Earthquake Information Center reponse to the 11 March 2011 Mw 9.0 Tohoku earthquake, Seismol. Res. Lett. 82, 481-493, doi: 10.1785/gssrl.82.4.481.

Hayes, G.P., Wald, D.J., and Johnson, R.L., 2012a. Slab1.0: A three-dimensional model of global subduction zone geometries, J. Geophys. Res. 117, B01302, doi:10.1029/2011JB008524.

Hayes, G.P., Bergman, E., Benz, H.M., Johnson, K.L., Brown, L., and Melzner, A., 2012b. Seismotectonic framework of the February 27, 2010 Mw 8.8 Maule, Chile earthquake sequence, submitted to Geophys. J. Int., 10/2012.

Kagan, Y., 1991. 3-D rotation of double-couple earthquake sources, Geophys. J. Int., 106, 709–716.

Kanamori, H., and Rivera, L., 2008. Source inversion of W phase: speeding up seismic tsunami warning. Geophys. J. Int. 175, 222–238.

Kiser, E., and Ishii, M., 2011. The 2010 Mw 8.8 Chile earthquake: Triggering on multiple segments and frequency-dependent rupture behavior. Geophys. Res. Lett., 38, doi:10.10129/2011GL047140.

Lange, D., Tilmann, F., Barrientos, S.E., Contreras-Reyes, E., Methe, P., Moreno, M., Heit, B., Agurto, H., Bernard, P., Vilotte, J-P., and Beck, S., 2012. Aftershock seismicity of the 27 February 2010 Mw 8.8 Maule earthquake rupture zone, Ear. Planet. Sci. Lett. 317-318, 413-425.

Lay, T., Ammon, C.J., Kanamori, H., Koper, K.D., Sufri, O., and Hutko, A.R., 2010. Teleseismic inversion for rupture process of the 27 February 2010 Chile (Mw 8.8) earthquake, Geophys. J. Lett. 37, L13301, doi:10.1029/2010GL043379.

Lay, T., Kanamori, H., Ammon, C.J., Koper, K.D., Hutko, A.R., Ye, L., Yue, H., and Rushing, T.M., 2012. Depth-varying rupture properties of subduction zone megathrust faults. J. Geophys. Res., 117, doi:10.1029/2011JB009133.

Lin, J., and Stein, R.S., 2004. Stress triggering in thrust and subduction earthquakes, and stress interaction between the southern San Andreas and nearby thrust and strike-slip faults, J. Geophys. Res. 109, doi:10.1029/2003JB002607.

Lorito, S., Romano, F., Atzori, S., Tong, X., Avallone, A., McCloskey, J., Cocco, M., Boschi, E., and Piatanesi, A., 2011. Limited overlap between the seismic gap and coseismic slip of the great 2010 Chile earthquake, Nature Geo. 4, doi: 10.1038/NGEO1073.

Moreno, M., Rosenau, M., and Oncken, O., 2010. 2010 Maule earthquake slip correlates with pre-seismic locking of Andean subduction zone, Nature 467, doi:10.1038/nature09349.

Moreno, M., *et al.*, 2012. Toward understanding tectonic control on the Mw 8.8 Maule Chile earthquake, Ear. Planet. Sci. Lett. 321-322, 152-165.

Pollitz. F., Brooks, B., Tong, X., Bevis, M.F., Foster, J.H., Bürgmann, R., Smalley, R. Jr., Vigny, C., Socquet, A., Ruegg, J-C., Campos, J., Barrientos, S., Parra, H., Baez Soto, J.C., Cimbaro, S., and Blanco, M., 2011. Coseismic slip distribution of the February 27, 2010 Mw 8.8 Maule, Chile earthquake, Geophys. Res. Lett. 38, L09309, doi:10.1029/2011GL047065.

Rietbrock, A., Ryder, I., Hayes, G., Haberland, C., Comte, D., Roecker, S., and Lyon-Caen, H., 2012. Aftershock seismicity of the 2010 Maule Mw=8.8, Chile, earthquake: Correlation between co-seismic slip models and aftershock distribution?, Geophys. Res. Lett. 39, L08310, doi:10.1029/2012GL051308.

Ruegg, J.C., Rudloff, A., Vigny, C., Madariaga, R., de Chabalier, J.B., Campos, J., Kausel, E., Barrientos, S., and Dimitrov, D., 2009. Interseismic strain accumulation measured by GPS in the seismic gap between Constitución and Concepción in Chile, Phys. Ear. Planet. Int. 175, 78-85.

Ryder, I., Rietbrock, A., Kelson, K., Bürgmann, R., Floyd, M., Socquet, A., Vigny, C., and Carrizo, D., 2012. Large extensional aftershocks in the continental forearc triggered by the 2010 Maule earthquake, Chile, Geophys. J. Int 188, 879-890.

Shao, G., Li, X., Liu, Q., Zhao, X., Yano, T., and Ji, C., 2010. Preliminary slip model of the Feb 27, 2010 Mw 8.9 Maule, Chile Earthquake,
http://www.geol.ucsb.edu/faculty/ji/big_earthquakes/2010/02/27/chile_2_27.html.

Sladen, A., 2010. Preliminary result 02/27/2010 (Mw 8.8), Chile, http://tectonics.caltech.edu/slip_history/2010_chile/index.html.

Tong, X., Sandwell, D., Luttrell, K., Brooks, B., Bevis, M., Shimada, M., Foster, J., Smalley, R. Jr., Parra, H., Báez Soto, J.C., Blanco, M., Kendrick, E., Genrich, J., and Cassamise II, D.J., 2010. The 2010 Maule Chile earthquake: Downdip rupture limit revealed by space geodesy, Geophys. Res. Lett. 37, L24311, doi:10.1029/2010GL045805.

Vigny, C., *et al.*, 2011. The 2010 Mw 8.8 Maule Megathrust Earthquake of Central Chile, Monitored by GPS, Science 332, doi: 10.1126/science.1204132.

Wang, D., and Mori, J., 2011. Frequency-dependent energy radiation and fault coupling for the 2010 Mw 8.8 Maule, Chile, and 2011 Mw 9.0 Tohoku, Japan, earthquakes. Geophys. Res. Lett., 38, doi:10.1029/2011GL049652.